


Design and Experimental Demonstration of Impedance-Matched Circular-Polarization-Selective Surfaces with Spin-Selective Phase Modulations

Minseok Kim^{✉*} and George V. Eleftheriades[†]

The Edward S. Rogers Department of Electrical and Computer Engineering, University of Toronto, Toronto, Canada

 (Received 8 September 2019; revised manuscript received 17 November 2019; published 7 January 2020)

We present the design and experimental demonstration of an impedance-matched circular-polarization-selective surface that also offers spin-selective phase modulations at microwave frequencies. We achieve this by leveraging the theory of Pancharatnam-Berry phase shift and cascading four tensor impedance layers, each comprising an array of crossed meander lines. These meander lines are precisely tuned and rotated to implement particular tensor surface impedance values to satisfy the impedance-matching condition for the transmitted right-handed circularly polarized field while inducing Pancharatnam-Berry phase shift for only the reflected left-handed circularly polarized field. We present a detailed numerical synthesis technique to obtain the required impedance values to satisfy the impedance-matching condition, and demonstrate spin-selective phase modulations based on Pancharatnam-Berry phase shifts. To verify the proposed idea, we experimentally demonstrate nearly reflectionless transmission of right-handed circular polarization at broadside and reflection of left-handed circular polarization at 33° off broadside at 12 GHz. For this purpose, a free-space quasi-optical setup and a near-field measurement system are used to measure the transmitted and reflected circularly polarized fields, respectively.

DOI: [10.1103/PhysRevApplied.13.014009](https://doi.org/10.1103/PhysRevApplied.13.014009)

I. INTRODUCTION

The idea of full control of the reflective and transmissive properties of electromagnetic (EM) waves has triggered huge research interest from both the physics community and the engineering community due to its numerous potential applications. In this regard, recent years have witnessed rapid development in the field of metasurfaces, which are artificial EM surfaces comprising arrays of subwavelength-sized unit cells. By engineering of the local interaction properties between the unit cells and an incident EM field, metasurfaces for various applications have been proposed to date [1–8]. For example, phase-gradient metasurfaces have been demonstrated for applications such as light bending [1–4,9], holograms [10–12], and orbital-angular-momentum generation [13–15]. In these phase-gradient metasurfaces, unit cells are tailored to provide certain reflection or transmission phase profiles along the surfaces such that they locally match the tangential wave vectors for anomalously reflected or refracted fields. As such, much effort has been placed on the demonstrations of unit cells that provide a full range of 360° of transmission or reflection phase shifts. In parallel to these studies, metasurfaces that arbitrarily control the polarization state of the scattered waves have also

been extensively studied. For example, numerous metasurfaces that leverage birefringence have been reported for devices such as quarter-wave and half-wave plates [6,16–18]. These birefringent metasurfaces, however, have limited polarization control of EM waves in the sense that they fail to control the flow (e.g., phase velocity) of different circular polarizations (CPs). To also control the flow of both left-handed circular polarization (LHCP) and right-handed circular polarization (RHCP), chiral metasurfaces have been demonstrated that involve the use of uniform bianisotropic unit cells. Among various chiral polarization transformations, CP selectivity has gained particular interest owing to its promising applications in areas such as satellite communications [19]. In particular, Zhao *et al.* [20,21] have captured much attention with their proposal for a “twisted-metamaterial” for realization of a circular-polarization-selective surface (CPSS) that transmits one handedness of a CP field while reflecting the opposite handedness. The proposed multilayer scheme consists of cascaded layers of identical unit cells that are progressively rotated along the propagation direction of an incident field. In this respect, their operation is akin to mimicking a helical structure, which is a known geometry for chiral molecules found in nature [20–22]. As such, they are not necessarily optimal in the sense that they are not guaranteed to be impedance matched, which can lead to degraded efficiency from undesired reflections, because they rely merely on a rotated-lattice effect to naturally

*minseok.kim@mail.utoronto.ca

†geleft@ece.utoronto.ca

realize chirality. On the other hand, subsequent work by Selvanayagam *et al.* demonstrated a systematic method to realize an impedance-matched CPSS by cascading two surfaces with both electric and magnetic polarizations [23] and cascading three surfaces with only electric polarizations [24]. Following these studies, other researchers proposed a similar multilayered structure where each impedance layer is precisely optimized for realization of a broadband CPSS [25,26]. Additionally, Kim and Eleftheriades [27] demonstrated an impedance-matched CPSS that operates at two user-defined frequencies by cascading dual-resonance tensor impedance surfaces.

Although these previous CPSSs were successfully demonstrated, they commonly use uniform unit-cell arrays. As a result, other than a polarization transformation, they cannot perform arbitrary beam shaping for the reflected or transmitted CP fields. However, a CPSS that also combines the functions of phase-gradient metasurfaces is of great interest in many applications (e.g., multiple-beam formation in satellite communications). In this regard, researchers have recently started to report a few chiral metasurfaces that can also reshape the reflected or transmitted CP fields. For example, at the cost of increased complexity in fabrication, a curved CPSS was demonstrated in Ref. [28], where the CPSS is physically shaped to obtain the necessary reflection phase shifts from the wave propagation. On the other hand, planar phase-gradient chiral metasurfaces have also been demonstrated that take advantage of the geometrical phase shift [29–32]. In particular, these phase-gradient chiral metasurfaces realize spin-selective phase modulations by rotating individual chiral unit cells to acquire the Pancharatnam-Berry phase shifts along their surfaces [33]. On the basis of this principle, Jing *et al.* [30] demonstrated absorption for one handedness of a CP field and arbitrary reflection for the other handedness. A phase-gradient CPSS that normally reflects an incident LHCP field while applying arbitrary transmission phase shift for an incident RHCP field was demonstrated in Ref. [32]. Despite their successful demonstrations, however, none of these previous studies have shown a systematic way to also satisfy the impedance-matching condition for the transmitted CP fields while maximizing the reflection for the opposite handedness. In this sense, they do not possess optimal efficiency as they do not offer a means to suppress any unwanted reflections or transmissions for their surfaces.

In departure from the aforementioned studies, we here propose and experimentally demonstrate a CPSS that is precisely designed to (i) satisfy the impedance-matching condition for the transmitted RHCP field and (ii) induce spin-selective phase modulations for the reflected LHCP field. We achieve this by leveraging the theory of Pancharatnam-Berry phase shift and cascading four tensor impedance layers in which each layer precisely implements particular impedance values. Whereas the

preliminary numerical results were reported in Ref. [34], this study shows the detailed numerical synthesis method for obtaining the required impedance values by modeling the four-layered system in a multiconductor transmission line. The computed surface impedances are then physically encoded by use of rotated crossed meander lines as the unit cells at microwave frequencies (12 GHz). The proposed unit cell can implement a large range of either capacitance or inductance for two orthogonal linearly polarized (LP) waves. Moreover, the unit cell does not rely on any resonances for accessing these capacitances or inductances, thereby minimizing Ohmic losses. On the basis of the proposed unit cell, we numerically and experimentally demonstrate a case where an incident LHCP field is fully reflected at a certain prescribed angle, while an incident RHCP field is transmitted with minimum reflection. In particular, we use a free-space quasi-optical system to measure the transmission of a RHCP field and a near-field measurement system to verify anomalous reflection of a LHCP field. The demonstrated example is of particular interest in many applications such as CP detectors, polarizers, spin-selective orbital-angular-momentum generation, and multiple-beam generation for satellite communications.

II. DESIGN OF AN IMPEDANCE-MATCHED CPSS WITH SPIN-SELECTIVE PHASE MODULATIONS

The objective of this paper is to realize an ideal CPSS that is (i) impedance matched and (ii) offers spin-selective phase modulations. To this end, we consider cascading four impedance layers similar to our previous work in [24,27,35] that demonstrated uniform chiral metasurfaces (i.e., a constant magnitude and phase for the reflected and transmitted CP fields). Previously, it was theoretically shown that three cascaded lossless impedance layers are sufficient to synthesize an impedance-matched CPSS [24]. However, with only three impedance layers, some of the required impedance values can be difficult to synthesize (e.g., they are highly capacitive or inductive), and the impedance layers often need to behave like a short circuit (i.e., highly reflective). In these cases, any small Ohmic losses can significantly degrade the overall performance, which is highly undesirable. To overcome this issue, here we use an additional impedance layer as shown in Fig. 1, where each layer is represented by an ideal tensor impedance surface in a multiconductor-transmission-line system. In what follows, Sec. II A discusses the numerical synthesis method for an impedance-matched CPSS based on the proposed multilayered scheme. Section II B then discusses the physical realization of an impedance-matched CPSS, which we later use as a building block to demonstrate spin-selective phase modulations in Sec. II C.

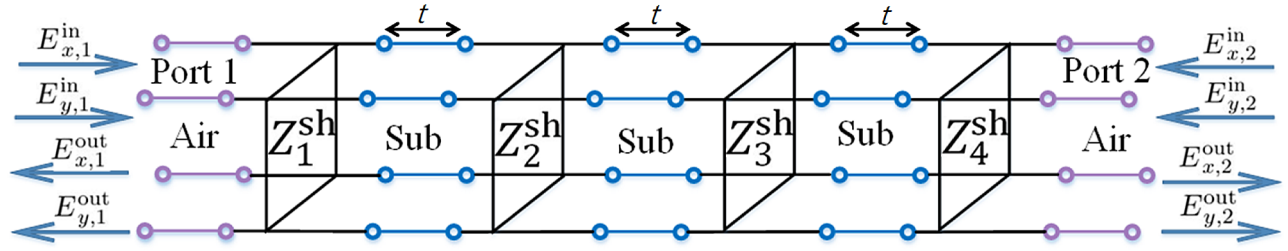


FIG. 1. The impedance-matched CPSS in a multiconductor-transmission-line system. The system effectively consists of four ports: two for the physical ports and the other two for the orthogonal-polarization states. The superscripts “in” and “out” denote whether a field is an input or an output, respectively. The subscripts x and y represent the polarization states of the fields. Specifically, x and y respectively represent LP fields that are polarized along the x and y directions. The subscript numbers, 1 and 2, denote the physical port numbers.

A. Numerical synthesis of an impedance-matched CPSS

To synthesize an impedance-matched CPSS based on the proposed four cascaded tensor impedance layers shown in Fig. 1, we first envision its net scattering matrix, \mathbf{S}_{UC} , as

$$\begin{aligned} \mathbf{S}_{UC} &= \begin{pmatrix} S_{11}^{xx} & S_{11}^{xy} & S_{12}^{xx} & S_{12}^{xy} \\ S_{11}^{yx} & S_{11}^{yy} & S_{12}^{yx} & S_{12}^{yy} \\ S_{21}^{xx} & S_{21}^{xy} & S_{22}^{xx} & S_{22}^{xy} \\ S_{21}^{yx} & S_{21}^{yy} & S_{22}^{yx} & S_{22}^{yy} \end{pmatrix} \\ &= \frac{1}{2} \begin{pmatrix} -1 & i & 1 & -i \\ i & 1 & i & 1 \\ 1 & i & -1 & -i \\ -i & 1 & -i & 1 \end{pmatrix} e^{j\xi}, \end{aligned} \quad (1)$$

where ξ represents an arbitrary phase constant. The subscript UC stands for ‘unit cell’ since we later utilize an impedance-matched CPSS as our unit cell for realization of spin-selective phase modulations. The scattering matrix in Eq. (1) is in a LP basis and it is defined as (referring to Fig. 1)

$$\begin{pmatrix} E_{x,1}^{\text{out}} \\ E_{y,1}^{\text{out}} \\ E_{x,2}^{\text{out}} \\ E_{y,2}^{\text{out}} \end{pmatrix} = \begin{pmatrix} S_{11}^{xx} & S_{11}^{xy} & S_{12}^{xx} & S_{12}^{xy} \\ S_{11}^{yx} & S_{11}^{yy} & S_{12}^{yx} & S_{12}^{yy} \\ S_{21}^{xx} & S_{21}^{xy} & S_{22}^{xx} & S_{22}^{xy} \\ S_{21}^{yx} & S_{21}^{yy} & S_{22}^{yx} & S_{22}^{yy} \end{pmatrix} \begin{pmatrix} E_{x,1}^{\text{in}} \\ E_{y,1}^{\text{in}} \\ E_{x,2}^{\text{in}} \\ E_{y,2}^{\text{in}} \end{pmatrix}, \quad (2)$$

where the scattering parameters in a LP basis are defined as

$$S_{ij}^{\alpha\beta} = \left. \frac{E_{\alpha,i}^{\text{out}}}{E_{\beta,j}^{\text{in}}} \right|_{E_{\kappa \neq \beta,l}^{\text{in}} = 0}. \quad (3)$$

In Eq. (3), α and β represent the direction of linear polarizations (i.e., either x or y), or equivalently different propagating modes at the output port (port i) and the input port (port j), respectively. The condition $E_{\kappa \neq \beta,l}^{\text{in}} = 0$ ensures the only input is $E_{\beta,j}^{\text{in}}$.

By multiplication of Eq. (1) by the Jones matrices for an incident LHCP field and RHCP field from port 1 or port 2, it can be readily shown that the transmission magnitude of a RHCP field is identically 1 (i.e., impedance matched and lossless), while that of a LHCP field is identically 0 (i.e., perfect reflection). Furthermore, the axial ratio for the transmitted RHCP field and the reflected LHCP field ideally remains unity, which implies that a RHCP field is transmitted into a pure RHCP field, while a LHCP field is reflected as a pure LHCP field. Therefore, \mathbf{S}_{UC} in Eq. (1) is our desired net scattering matrix for the cascaded system, and the goal here is to obtain the required surface impedance values in each layer such that they cascade to match to \mathbf{S}_{UC} .

To obtain the required surface impedance values, we first modularize each component in the proposed four-layered system shown in Fig. 1. In particular, we modularize the system into two main parts: (i) the transmission-line module and (ii) the tensor-impedance-layer module. The first module describes the wave propagation between the tensor impedance layers, and it can be mathematically represented by its scattering matrix, \mathbf{S}_{TL} , which is given as

$$\mathbf{S}_{TL} = \begin{pmatrix} 0 & 0 & e^{-ik_0 t n_{\text{sub}}} & 0 \\ 0 & 0 & 0 & e^{-ik_0 t n_{\text{sub}}} \\ e^{-ik_0 t n_{\text{sub}}} & 0 & 0 & 0 \\ 0 & e^{-ik_0 t n_{\text{sub}}} & 0 & 0 \end{pmatrix}, \quad (4)$$

where k_0 , t , and n_{sub} , respectively, represent the wave vector, separation length, and refractive index of the material between the impedance layers. For the remainder of this work, we assume that t is fixed to 3.175 mm and the material between the layers is a Rogers 5880 substrate (dielectric permittivity of 2.2). On the other hand, the second module, which describes the n th tensor impedance layer, can also be represented by its scattering matrix, \mathbf{S}_n , which is given as

$$\mathbf{S}_n = \mathbf{G}_n^{\text{ref}} \cdot (\mathbf{Z}_n^{\text{sh}} - \mathbf{Z}_n^{\text{ref}}) \cdot (\mathbf{Z}_n^{\text{sh}} + \mathbf{Z}_n^{\text{ref}})^{-1} \cdot \mathbf{G}_n^{\text{ref}-1}, \quad (5)$$

where $\mathbf{Z}_n^{\text{ref}}$ and $\mathbf{G}_n^{\text{ref}}$ are 4×4 diagonal matrices whose nonzero components are the reference-port impedances and normalized-port admittances for the n th layer, respectively. For example, $\mathbf{Z}_1^{\text{ref}}$ and $\mathbf{G}_1^{\text{ref}}$ for the first layer that faces air at port 1 and the substrate at port 2 are given as

$$\mathbf{Z}_1^{\text{ref}} = \begin{pmatrix} \eta_o & 0 & 0 & 0 \\ 0 & \eta_o & 0 & 0 \\ 0 & 0 & \eta_o/n_{\text{sub}} & 0 \\ 0 & 0 & 0 & \eta_o/n_{\text{sub}} \end{pmatrix}, \quad (6a)$$

$$\mathbf{G}_1^{\text{ref}} = \begin{pmatrix} \frac{1}{\sqrt{\eta_o}} & 0 & 0 & 0 \\ 0 & \frac{1}{\sqrt{\eta_o}} & 0 & 0 \\ 0 & 0 & \sqrt{\frac{n_{\text{sub}}}{\eta_o}} & 0 \\ 0 & 0 & 0 & \sqrt{\frac{n_{\text{sub}}}{\eta_o}} \end{pmatrix}, \quad (6b)$$

where η_o represents the free-space wave impedance. Furthermore, \mathbf{Z}_n^{sh} in Eq. (5) represents the impedance matrix for the n th tensor impedance layer and it is defined as

$$\mathbf{Z}_n^{\text{sh}} = \begin{pmatrix} Z_n^{xx} & Z_n^{xy} & Z_n^{xx} & Z_n^{xy} \\ Z_n^{yx} & Z_n^{yy} & Z_n^{yx} & Z_n^{yy} \\ Z_n^{xx} & Z_n^{xy} & Z_n^{xx} & Z_n^{xy} \\ Z_n^{yx} & Z_n^{yy} & Z_n^{yx} & Z_n^{yy} \end{pmatrix}. \quad (7)$$

The impedance parameters in Eq. (7) relate the difference in the magnetic fields at the boundary formed by the n th tensor impedance layer to the continuous tangential electric field at the boundary. In other words, the impedance matrix given in Eq. (7) describes the ratio between the induced surface currents on the n th impedance layer and the tangential electric components of the incident and scattered fields on the n th layer. Hence, it is given [24] by

$$\begin{pmatrix} E_x \\ E_y \end{pmatrix} = \begin{pmatrix} Z_n^{xx} & Z_n^{xy} \\ Z_n^{yx} & Z_n^{yy} \end{pmatrix} \begin{pmatrix} -(H_y^+ - H_y^-) \\ H_x^+ - H_x^- \end{pmatrix}, \quad (8)$$

where the 2×2 impedance matrix can also be diagonalized as

$$\begin{pmatrix} Z_n^{xx} & Z_n^{xy} \\ Z_n^{yx} & Z_n^{yy} \end{pmatrix} = \mathbf{R}(\theta) \begin{pmatrix} Z_n^X & 0 \\ 0 & Z_n^Y \end{pmatrix} \mathbf{R}^{-1}(\theta). \quad (9)$$

In Eq. (9), Z_n^X and Z_n^Y are the eigenvalues of the 2×2 impedance matrix in Eq. (8) and \mathbf{R} is a square matrix whose columns are the linearly independent eigenvectors of the 2×2 impedance matrix. Physically speaking, \mathbf{R} is

a 2×2 rotational matrix and θ is the angle by which the whole layer is rotated. Therefore, it is of the form given by

$$\mathbf{R}(\theta) = \begin{pmatrix} \cos \theta & -\sin \theta \\ \sin \theta & \cos \theta \end{pmatrix}. \quad (10)$$

Provided that these impedance parameters in each layer are known, the scattering matrices that describe each module can be constructed on the basis of Eqs. (4) and (5). With all these scattering matrices, the net scattering matrix of the overall cascaded system can then be obtained by cascading them via the generalized-scattering-matrix method. For example, two modules that are represented as \mathbf{S}^E and \mathbf{S}^F can be cascaded as

$$\mathbf{S}_{11}^{EF} = \mathbf{S}_{11}^E + \mathbf{S}_{12}^E (\mathbf{I} - \mathbf{S}_{11}^F \mathbf{S}_{22}^E)^{-1} \mathbf{S}_{11}^F \mathbf{S}_{21}^E, \quad (11a)$$

$$\mathbf{S}_{12}^{EF} = \mathbf{S}_{12}^E (\mathbf{I} - \mathbf{S}_{11}^F \mathbf{S}_{22}^E)^{-1} \mathbf{S}_{12}^F, \quad (11b)$$

$$\mathbf{S}_{21}^{EF} = \mathbf{S}_{21}^F (\mathbf{I} - \mathbf{S}_{22}^E \mathbf{S}_{11}^F)^{-1} \mathbf{S}_{21}^E, \quad (11c)$$

$$\mathbf{S}_{22}^{EF} = \mathbf{S}_{22}^F + \mathbf{S}_{21}^F (\mathbf{I} - \mathbf{S}_{22}^E \mathbf{S}_{11}^F)^{-1} \mathbf{S}_{22}^E \mathbf{S}_{12}^F, \quad (11d)$$

which arise by taking proper account for all reflected and transmitted field vectors between the two modules [36]. Here \mathbf{S}_{11}^{EF} , \mathbf{S}_{12}^{EF} , \mathbf{S}_{21}^{EF} , and \mathbf{S}_{22}^{EF} are 2×2 submatrices that form the net scattering matrix, \mathbf{S}^{EF} , which is in the following form:

$$\mathbf{S}^{EF} = \begin{pmatrix} S_{11}^{xx} & S_{11}^{xy} & S_{12}^{xx} & S_{12}^{xy} \\ S_{11}^{yx} & S_{11}^{yy} & S_{12}^{yx} & S_{12}^{yy} \\ S_{21}^{xx} & S_{21}^{xy} & S_{22}^{xx} & S_{22}^{xy} \\ S_{21}^{yx} & S_{21}^{yy} & S_{22}^{yx} & S_{22}^{yy} \end{pmatrix} = \begin{pmatrix} \mathbf{S}_{11}^{EF} & \mathbf{S}_{12}^{EF} \\ \mathbf{S}_{21}^{EF} & \mathbf{S}_{22}^{EF} \end{pmatrix}. \quad (12)$$

The discussion thus far has demonstrated how the net scattering matrix of the cascaded layers can be obtained by modularizing each component to its corresponding scattering matrix. However, we have not yet specified the required impedance values in each layer that would cascade to result in the desired net scattering matrix in Eq. (1). Although there is no closed-form solution for such a problem, there are several semianalytical methods to obtain these impedance values. For example, one can solve the algebraic Riccati equation as demonstrated in Ref. [24], which is similar to an impedance-matching problem, or use the nonlinear optimization method as outlined in Refs. [25,27,35]. The two methods are equally valid and we use the latter method to solve the problem. Specifically, we use MATLAB's built-in optimizer `fmincon` to find a minimum of the cost function, which is defined as

$$C = \max(|\mathbf{S}_{\text{net}} - \mathbf{S}_{\text{UC}}|), \quad (13)$$

where \mathbf{S}_{net} represents the net scattering matrix of the cascaded layers, which involves varying all possible values of

TABLE I. Optimized tensor impedance values.

	Layer 1	Layer 2	Layer 3	Layer 4
Z^X (Ω)	$i400$	$-i256$	$-i256$	$i400$
Z^Y (Ω)	$-i240$	$i40$	$i40$	$-i240$
θ (deg)	64.4	18.5	-18.5	-64.4

the impedance parameters in each layer. Similarly to the cost function used in Ref. [25] for realization of a broadband CPSS, we can modify the current cost function in Eq. (13) as

$$C = \frac{1}{f_2 - f_1} \int_{f_1}^{f_2} \max(|S_{\text{net}} - S_{\text{UC}}|) df \quad (14)$$

to also optimize it for a broad bandwidth. Nevertheless, since the goal of this work is not related to broadening the bandwidth of a CPSS, we take Eq. (13) as our cost function for convenience to focus on the demonstration of an impedance-matched CPSS that also offers spin-selective phase modulations. As shown later, however, the proposed method for realizing a spin-selective phase modulation (discussed in Sec. II C) does not depend on the frequency of operation. As such, the choice of a cost function does not influence the proposed method in this work. Additionally, in optimizing S_{net} , there are a total of 12 variables [two eigenvalues and one rotation angle per tensor impedance layer; see Eq. (9)]. Nonetheless, we can dramatically reduce the number of variables by invoking the C_4 -symmetry condition. Specifically, we set the eigenvalues of the first and last layers to be the same and their rotation angles to be $+\theta_a$ and $-\theta_a$, respectively. Similarly, we force the eigenvalues of the second and third layers to be the same and their rotation angles to be $+\theta_b$ and $-\theta_b$, respectively. On the basis of this scheme, only the rotation angles and eigenvalues of the first and second layers are optimized at the operating frequency of 12 GHz and the cost function is minimized to 0.0237. These optimized values are summarized in Table I.

B. Physical design of an impedance-matched CPSS

Whereas in the previous section we discussed a numerical synthesis method for obtaining the required surface impedances, in this section we discuss the physical realization of these required impedances. To this end, we propose crossed meander lines as our unit cells to form each layer. The top views of the proposed unit cells that form the first and second layers are shown in Figs. 2(a) and 2(b), respectively. The unit-cell periodicity is 4.5 mm (approximately $\lambda/5.5$) and the unit cells are printed on 3.175-mm-thick Rogers 5880 substrates. They are also bonded with 0.0508-mm-thick Rogers 2929 bondplies to form the proposed cascaded tensor impedance layers as shown in Fig. 2(c), producing an overall thickness of approximately 9.55 mm

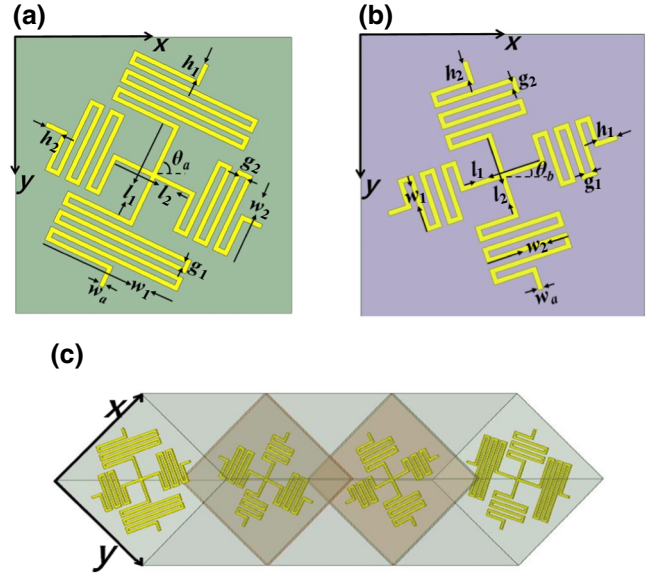


FIG. 2. The proposed unit cells. (a),(b) Top views of the unit cells that implement the optimized tensor impedance values in the first and second layers and (c) the cascaded unit cells. The first (or the second) and the last (or the third) layers are identical except that they are rotated in mirror symmetry.

(approximately $\lambda/2.6$). While thinner substrates could be used to realize more-compact designs, we purposely use thick substrates to obtain a sturdier structure. However, the substrates cannot be indefinitely thin because the proposed theory does not take interlayer mutual coupling into account, as we assume that only two fundamental Floquet modes are propagating between the impedance layers. In Ref. [21], a detailed discussion regarding such mutual coupling is given, and the Appendix presents the coupling analysis based on the proposed unit-cell design. The analysis in the Appendix shows that the mutual coupling can be mostly eliminated by use of substrates that are thicker than 2.5 mm.

To relate the physical geometries of the proposed unit cells to the required impedance values in Table I, we simulate the unit cells shown in Figs. 2(a) and 2(b) for $\theta_a = \theta_b = 0^\circ$ [to relate them to Z_n^X and Z_n^Y in Eq. (9)] and for various lengths of the meander lines. Specifically, the unrotated unit cells with various lengths of the meander lines are simulated in ANSYS High Frequency Structure Simulator (HFSS), with a periodic boundary condition and Floquet port excitations. The impedance parameters of the unit cells are then computed via HFSS simulations, which are in the form of $Z_{\text{HFSS}}[\text{output port } i, \text{output mode } \alpha, \text{input port } j, \text{input mode } \beta]$. These impedance parameters can be related to the eigenvalues in Eq. (9) (i.e., Z_n^X and Z_n^Y) as

$$Z_n^\alpha = Z_{\text{HFSS}}[2, \alpha, 1, \alpha], \quad (15)$$

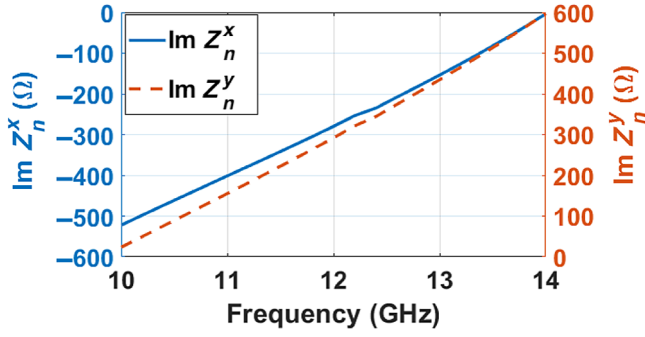


FIG. 3. The frequency response of the proposed unit cell.

where, again, α represents the direction of linear polarization (i.e., x and y). By changing the overall lengths of the crossed meander lines and their number of turns, we can independently and widely tune Z_n^X and Z_n^Y as shown in Fig. 3. Specifically, Fig. 3 shows an example of the variation in Z_n^X and Z_n^Y near the operating frequency of 12 GHz. As seen, the unit-cell response for an x -polarized field (shown as a solid blue curve) can be capacitive, ranging from $-i500$ to 0Ω , while that of a y -polarized field (shown as a dotted red curve) can be inductive, ranging from 0 to $i600 \Omega$. Because the unit cell offers an independent tuning of the surface impedances for the two orthogonal LP fields, with a wide range of capacitances and inductances, we can conveniently translate the required Z_n^X and Z_n^Y in Table I to their corresponding physical structures. Furthermore, as shown in Fig. 3, the unit cell does not rely on any resonances, which also allows minimization of Ohmic losses. However, this off-resonance operation does not necessarily guarantee a broadband CPSS because the demonstrated chirality (i.e., CP selectivity) results from the cascaded unit cells. For the devised CPSS, its bandwidth is narrow because the separation lengths between the impedance layer depend on the frequency of operation. To also realize a broadband operation, however, one can modify the cost function similarly to Eq. (14).

By precisely tuning the crossed meander lines, we sample the required Z_n^X and Z_n^Y in Table I. These optimized unit cells are then rotated by the required rotation angles (i.e., θ in Table I) and cascaded to physically realize an impedance-matched CPSS as shown in Fig. 2(c). The physically realized surface impedance values from the rotated unit cells are compared with the required ones in Table II.

As seen, the reactance values of the proposed unit cells almost perfectly match the desired ones with small resistances. The corresponding geometrical parameters of the unit cells are summarized in Table III.

On the basis of the cascaded physical unit cells, we perform a full-wave simulation to verify the physically realized impedance values. For this, the insertion loss (T),

TABLE II. Comparison between the physically realized surface impedance values from the proposed unit cells and the required values in Table I.

		Physical	Numerical
Layer 1	$Z_1^{xx} (\Omega)$	$(7 - i122)$	$-i120$
	$Z_1^{yy} (\Omega)$	$(11.13 + i281)$	$i280$
	$Z_1^{xy} = Z_1^{yx} (\Omega)$	$(2.79 + i247)$	$i250$
Layer 2	$Z_2^{xx} (\Omega)$	$(4.75 - i225.6)$	$-i226$
	$Z_2^{yy} (\Omega)$	$(6.7 + i13.32)$	$i10$
	$Z_2^{xy} = Z_2^{yx} (\Omega)$	$(0.76 - i90)$	$-i89$

return loss (R), and axial ratio (A) of the reflected and transmitted CP fields are examined as shown in Fig. 4. These three figures of merit are extracted by first converting the net scattering matrix obtained from the full-wave simulation (which is in a LP basis) to a scattering matrix in a CP basis as given by

$$\begin{aligned}
 & \begin{pmatrix} S_{11}^{RR} & S_{11}^R & S_{12}^{RR} & S_{12}^R \\ S_{11}^{LR} & S_{11}^{LL} & S_{12}^{LR} & S_{12}^{LL} \\ S_{21}^{RR} & S_{21}^R & S_{22}^{RR} & S_{22}^R \\ S_{21}^{LR} & S_{21}^{LL} & S_{22}^{LR} & S_{22}^{LL} \end{pmatrix} \\
 &= \frac{1}{2} \begin{pmatrix} 1 & -i & 0 & 0 \\ 1 & i & 0 & 0 \\ 0 & 0 & 1 & i \\ 0 & 0 & 1 & -i \end{pmatrix} \begin{pmatrix} S_{11}^{xx} & S_{11}^{xy} & S_{12}^{xx} & S_{12}^{xy} \\ S_{11}^{yx} & S_{11}^{yy} & S_{12}^{yx} & S_{12}^{yy} \\ S_{21}^{xx} & S_{21}^{xy} & S_{22}^{xx} & S_{22}^{xy} \\ S_{21}^{yx} & S_{21}^{yy} & S_{22}^{yx} & S_{22}^{yy} \end{pmatrix} \\
 & \times \begin{pmatrix} 1 & 1 & 0 & 0 \\ -i & i & 0 & 0 \\ 0 & 0 & 1 & 1 \\ 0 & 0 & i & -i \end{pmatrix}, \quad (16)
 \end{aligned}$$

where the scattering parameters in a CP basis are defined as

$$S_{ij}^{pq} = \left. \frac{E_{p,i}^{\text{out}}}{E_{q,j}^{\text{in}}} \right|_{E_{\kappa \neq q,l}^{\text{in}} = 0}, \quad (17)$$

where S_{ij}^{pq} is the ratio between the output CP (its handedness depends on p ; $p = R$ or L for RHCP or LHCP,

TABLE III. Physical geometries of the unit cells that implement the required impedance values in Table I.

	w_1 (mm)	w_2 (mm)	g_1 (mm)	g_2 (mm)	l_1 (mm)
Layer 1	2.313	1.365	0.08	0.1	1.658
Layer 2	0.9362	1.363	0.1	0.1	1.271
	l_2 (mm)	h_1 (mm)	h_2 (mm)	w_a (mm)	θ (deg)
Layer 1	1.329	0.3	0.3	0.08	64.4
Layer 2	1.271	0.3	0.3m	0.08	18.5

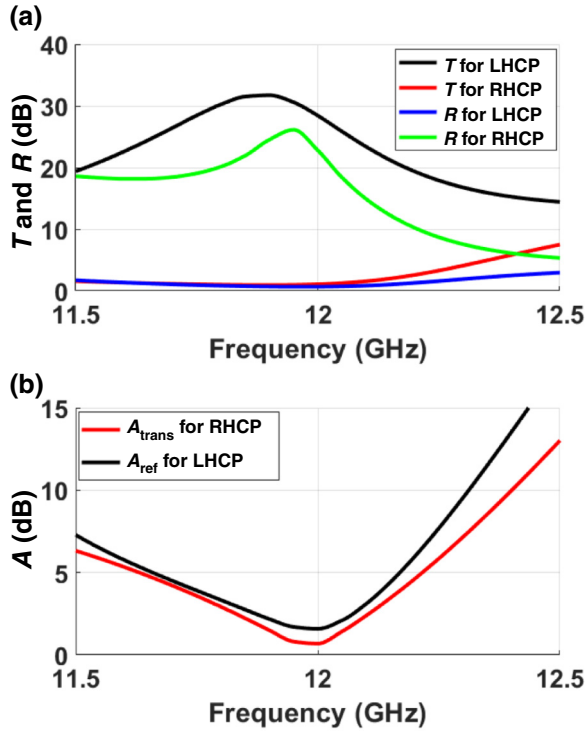


FIG. 4. Full-wave simulation results. (a) The insertion and return loss and (b) the axial ratios for the reflected LHCP field (A_{ref}) and the transmitted RHCP field (A_{trans}).

respectively) at port i to the input CP ($q = R$ or L for RHCP or LHCP, respectively) at port j assuming that it is the only input. On the basis of these scattering parameters in a CP basis, we define T , R , and A of the reflected and transmitted CP fields. Specifically, the T (insertion loss) quantifies how well a CPSS transmits a certain CP field. Hence, it is defined as

$$T = -20 \log_{10} |S_{ij}^{pp}|, \quad i \neq j. \quad (18)$$

On the other hand, the R (return loss) quantifies how well a CPSS reflects the other handedness. Hence, it is defined as

$$R = -20 \log_{10} |S_{ii}^{pp}|. \quad (19)$$

Lastly, the A (axial ratio), which defines the ratio between the major and minor axes of the polarization ellipse for the reflected and transmitted CP fields, is given as [37,38]

$$A = 20 \log_{10} \left(\frac{\sqrt{\sqrt{1 + \kappa} + 1}}{\sqrt{\sqrt{1 + \kappa} - 1}} \right), \quad (20)$$

where κ is given as

$$\kappa = \frac{1}{4} \left(\left| \frac{S_{ii}^{pq}}{S_{ii}^{qq}} \right| - \left| \frac{S_{ii}^{qq}}{S_{ii}^{pq}} \right| \right) \quad (21)$$

As seen from Fig. 4, the net scattering matrix of the cascaded unit cells closely matches Eq. (1) since the insertion and return losses of RHCP and LHCP fields are merely 1.15 and 0.69 dB, respectively, at the design frequency of 12 GHz (with all the material losses included in the simulation). On the other hand, the return loss of a RHCP field is 23.62 dB, which implies that the structure is virtually reflectionless for a RHCP field (i.e., impedance matched). In addition, the axial ratios of the reflected and transmitted CP fields are 1.56 and 1.25 dB, respectively. Therefore, the cascaded unit cells effectively transmit and reflect a particular handedness, while preserving the handedness of the reflected and reflected CP fields.

C. Realization of spin-selective phase modulations

Whereas in the previous subsection we discussed a physical design of an impedance-matched CPSS, in this subsection we use the devised impedance-matched CPSS as our building block to also demonstrate spin-selective phase modulations for reshaping of the CP fields. To reshape the scattered CP fields, one may consider repeating the previously demonstrated design procedure and solve for another desired scattering matrix with different ξ in Eq. (1). However, this will impose the same phase for the reflected and transmitted CP fields. In contrast, we are interested in obtaining a spin-selective phase modulation. For this purpose, we use the theory of Pancharatnam-Berry phase shift [39,40]. To understand how the theory can be used in the devised CPSS, we first envision an anisotropic unit cell that is rotated by some angle, γ . In particular, we consider a reflective anisotropic unit cell whose reflection coefficients for x -polarized and y -polarized waves are represented as r_x and r_y , respectively. Such a unit cell can be represented by its corresponding Jones matrix, \mathbf{M} , given as

$$\mathbf{M} = \begin{pmatrix} \cos \gamma & -\sin \gamma \\ \sin \gamma & \cos \gamma \end{pmatrix} \begin{pmatrix} r_x & 0 \\ 0 & r_y \end{pmatrix} \begin{pmatrix} \cos \gamma & \sin \gamma \\ -\sin \gamma & \cos \gamma \end{pmatrix}. \quad (22)$$

For an incident RHCP field and an incident LHCP field ($\vec{E}_{\text{inc}}^{R/L}$), the reflected field from the unit cell (\vec{E}_{ref}) is given by

$$\begin{aligned} \vec{E}_{\text{ref}} &= M \vec{E}_{\text{inc}}^{R/L} \\ &= \frac{r_x + r_y}{2} \vec{E}_{\text{inc}}^{L/R} + \frac{r_x - r_y}{2} \vec{E}_{\text{inc}}^{R/L} e^{i2m\gamma}, \end{aligned} \quad (23)$$

where m is either negative or positive for a right-handed or left-handed circularly polarized input field, respectively. It is seen from Eq. (23) that if r_x and r_y are of the same magnitude and they are out of phase by 180° (i.e., $r_x = -r_y$), then the reflection phase is exactly twice the unit cell's physical rotation angle, γ . Hence, a full 360° phase shift is realizable simply by rotating the anisotropic unit cell from

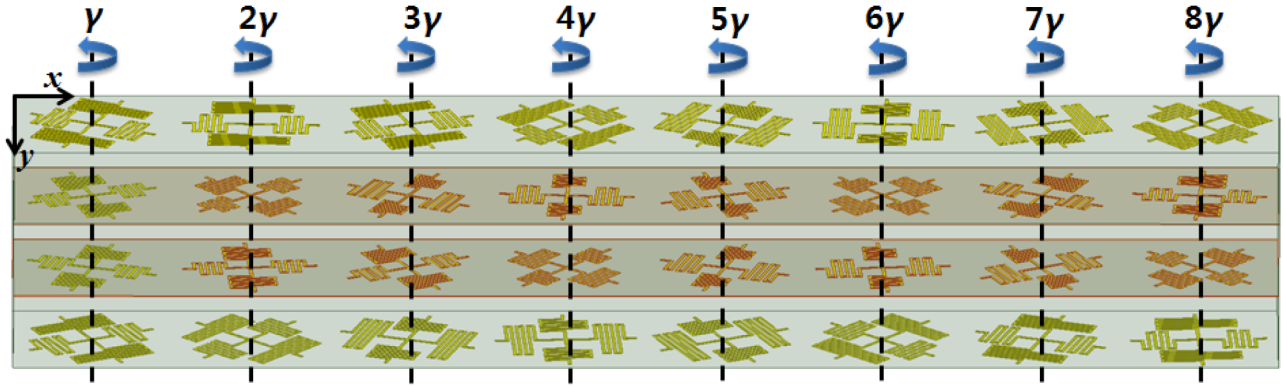


FIG. 5. An array of cascaded unit cells that are progressively rotated by γ along the lateral direction (i.e., x axis).

0° to 180° . On the basis of this knowledge, the first quadrant of \mathbf{S}_{UC} in Eq. (1) is compared with Eq. (22). From the comparison, it is readily seen that \mathbf{S}_{UC} also offers S_{11}^{xx} and S_{11}^{yy} that are of the same magnitude and they are also exactly 180° apart. Moreover, S_{11}^{xy} and S_{11}^{yx} are also identical to each other. Since the net scattering matrix of the cascaded unit cells closely matches \mathbf{S}_{UC} as verified from the previous analyses, the comparison implies that the cascaded unit cells are also capable of inducing a reflection phase based on the theory of Pancharatnam-Berry phase shift. To demonstrate this point, we consider an array of cascaded unit cells and progressively rotate them by γ as shown in Fig. 5. The local output from the n th cascaded unit cells for an incident LHCP field can be calculated as

$$\begin{aligned} \begin{pmatrix} E_{x,1}^{\text{out}} \\ E_{y,1}^{\text{out}} \\ E_{x,2}^{\text{out}} \\ E_{y,2}^{\text{out}} \end{pmatrix} &= \frac{1}{\sqrt{2}} \begin{pmatrix} \mathbf{R}(n\gamma) & \mathbf{0} \\ \mathbf{0} & \mathbf{R}(n\gamma) \end{pmatrix} \mathbf{S}_{\text{UC}} \\ &\quad \times \begin{pmatrix} \mathbf{R}(n\gamma) & \mathbf{0} \\ \mathbf{0} & \mathbf{R}(n\gamma) \end{pmatrix}^{-1} \begin{pmatrix} 1 \\ 0 \\ 0 \\ 0 \end{pmatrix} \\ &= \frac{1}{\sqrt{2}} \begin{pmatrix} 1 \\ -i \\ 0 \\ 0 \end{pmatrix} e^{i2n\gamma}, \end{aligned} \quad (24)$$

where $\mathbf{R}(n\gamma)$ is the 2×2 rotational matrix for the n th cascaded unit cells, for which its form is given in Eq. (10), and $\mathbf{0}$ represents a 2×2 null matrix. As seen, the output is a LHCP field (note the flip of the sign for $E_{y,1}^{\text{out}}$ since the wave is traveling in the negative z direction) that acquires a reflection phase shift that corresponds to exactly twice the physical rotation angle, $n\gamma$.

Whereas the reflected LHCP field acquires a reflection phase based on the theory of Pancharatnam-Berry phase shift, an incident RHCP field does not sense any physical

rotation because S_{21}^{xx} and S_{21}^{yy} are in phase. Specifically, the output for an incident RHCP field is given as

$$\begin{aligned} \begin{pmatrix} E_{x,1}^{\text{out}} \\ E_{y,1}^{\text{out}} \\ E_{x,2}^{\text{out}} \\ E_{y,2}^{\text{out}} \end{pmatrix} &= \frac{1}{\sqrt{2}} \begin{pmatrix} \mathbf{R}(n\gamma) & \mathbf{0} \\ \mathbf{0} & \mathbf{R}(n\gamma) \end{pmatrix} \mathbf{S}_{\text{UC}} \\ &\quad \times \begin{pmatrix} \mathbf{R}(n\gamma) & \mathbf{0} \\ \mathbf{0} & \mathbf{R}(n\gamma) \end{pmatrix}^{-1} \begin{pmatrix} 1 \\ 0 \\ 0 \\ 0 \end{pmatrix} = \frac{1}{\sqrt{2}} \begin{pmatrix} 0 \\ 0 \\ 1 \\ -i \end{pmatrix}, \end{aligned} \quad (25)$$

where it is seen that the transmitted field is still a RHCP field and it is the same as that of the case where $\gamma = 0^\circ$. Therefore, on the basis of the theory of Pancharatnam-Berry phase shift, we can selectively apply a phase shift for only the reflected LHCP field without affecting the transmitted RHCP field and still preserve the impedance-matching condition. This also implies that if one desires to also independently control the phase for the transmitted CP field, one can repeat the design procedure outlined in the previous subsection with a new value of ξ in Eq. (1) for the transmission phase shift and use the Pancharatnam-Berry phase for the reflection phase shift. However, for brevity, the remainder of this study considers a constant phase for the transmitted RHCP field such that the same physical cascaded unit cells can be used, where they can be simply rotated to selectively apply a certain phase shift only for the reflected CP field.

To verify the proposed idea for the spin-selective phase modulation, an array of eight cascaded unit cells (shown in Fig. 5) is simulated via use of HFSS. In particular, each of the cascaded unit cells is progressively rotated by $\gamma = 22.5^\circ$ in the lateral direction to encode a full 360° of reflection phase shift across the surface and reflect a normally incident LHCP field at 44° . The relationship between the rotation angle of the cascaded unit cells, γ , and the

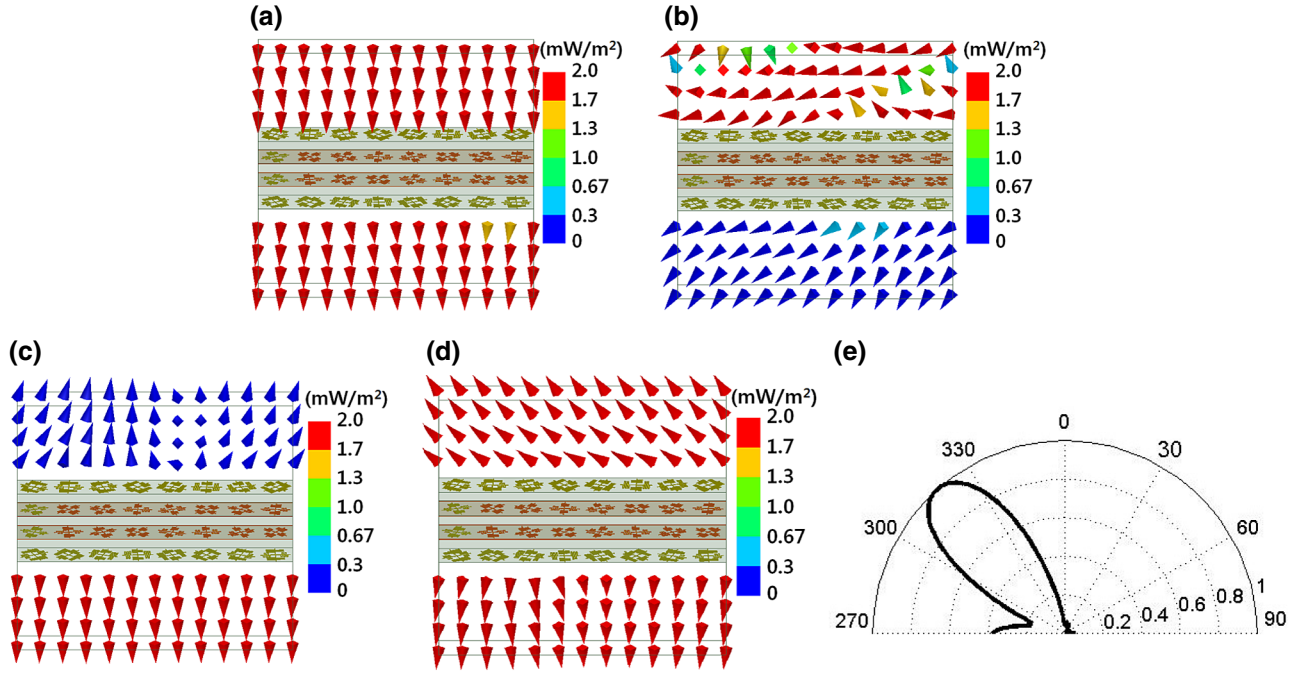


FIG. 6. The Poynting-vector distributions for the total fields and scattered fields, and the radiation pattern (based on the scattered field) of an array of the rotated cascaded unit cells. The Poynting vectors of the total fields in the case of (a) a normally incident RHCP field and (b) a normally incident LHCP field. The Poynting vectors of the scattered fields in the case of (c) a normally incident RHCP field and (d) a normally incident LHCP field. (e) The radiation pattern of the scattered field in case of a LHCP-field excitation.

reflected angle, θ_r , is given as

$$\theta_r = \sin^{-1} \left(\frac{\lambda_o \gamma}{\pi T} \right), \quad (26)$$

where it is assumed that the angle of incidence is zero (i.e., normal incidence) and T represents the unit-cell periodicity, which is set to 4.5 mm. The full-wave-simulation results are summarized in Fig. 6, where Figs. 6(a) and 6(b), respectively, show the Poynting vectors of the total fields (i.e., incident field plus scattered field) in the case of an incident RHCP field and an incident LHCP field. From Fig. 6(a), it is seen that an incident RHCP field does not sense the rotations of the cascaded unit cells as the surface is almost reflectionless to an incoming RHCP field. On the other hand, Fig. 6(b) shows that an incident LHCP field is mostly reflected and modulated as almost no field is present at the bottom of the surface. To further illustrate that an incident RHCP field is mostly transmitted with minimal reflection, while an incident LHCP field is mostly reflected at the prescribed reflection angle of 44° , Figs. 6(c) and 6(d), respectively, show the Poynting vectors of the scattered fields (i.e., total field minus incident field) in the case of an incident RHCP field and an incident LHCP field. From Fig. 6(c), it is seen that an incident RHCP field is normally transmitted and there is virtually no reflection from the array. In contrast, Fig. 6(d) shows high reflection of an incident LHCP field, which is also directed at

around 44° . At this point, it should be again reminded that the Poynting-vector distributions shown in Figs. 6(c) and 6(d) are those of the scattered fields (i.e., total field minus incident field). As such, the forward-scattering LHCP field shown in Fig. 6(d) does not mean that the surface transmits appreciable amounts of an LHCP field. As evident from Fig. 6(b), it simply corresponds to the incident field with 180° phase shift (as it is responsible for destructively interfering with the incident field such that the total field below the metasurface is zero). Finally, Fig. 6(e) shows the radiation pattern (based on the scattered field) of the array in the case of an incident LHCP field, from which it is seen that the reflected LHCP field is indeed directed at the prescribed reflection angle of 44° . As such, the full-wave simulation verifies that any desired reflection phases can be obtained simply by rotating the cascaded unit cells while still satisfying the impedance-matching condition for the transmitted CP field.

III. EXPERIMENTAL VERIFICATION

To further verify the proposed idea for the spin-selective phase modulation, we fabricate an array of the cascaded unit cells as shown in Fig. 7(a). In particular, each cascaded unit cell in the fabricated sample is progressively rotated by 18° in the lateral direction from 0° to 360° to reflect a normally incident LHCP field at 33° off broadside while normally transmitting an incident RHCP field.

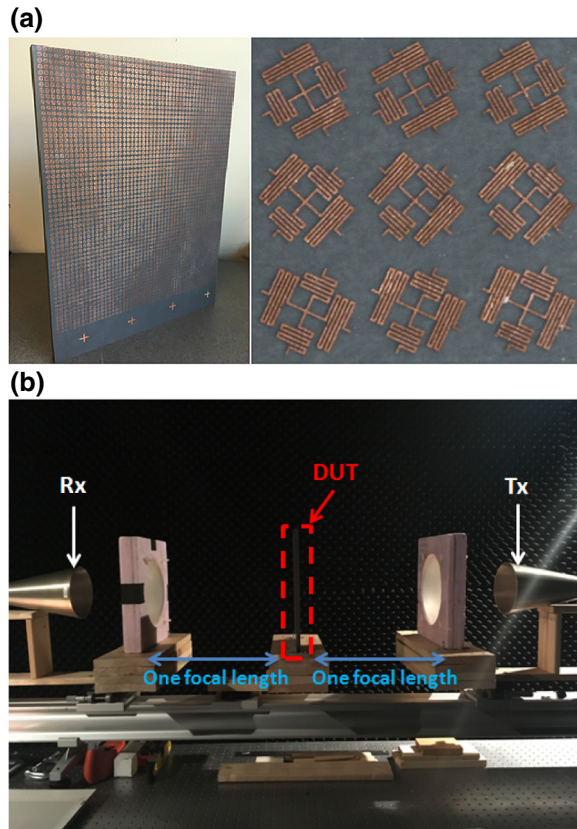


FIG. 7. The experimental setup for characterizing the transmission properties of the fabricated sample. (a) The fabricated sample and (b) the free-space quasi-optical measurement setup. DUT, device under test; Rx, receiving horn antenna; Tx, transmitting horn antenna.

Although a wider angle of reflection can be considered (as verified from the full-wave simulation with $\theta_r = 44^\circ$), we slightly reduce the reflection angle due to the measurement limitations. Moreover, while a rotation from 0° to 180° is sufficient for applying full 360° of reflection phase shift as evident from Eq. (24), we deliberately rotated it from 0° to 360° to avoid sudden structural changes at the phase wraps, which are known to cause the excitation of unwanted higher-order Floquet modes [41].

To measure the transmitted RHCP field, a quasi-optical measurement setup is used as shown in Fig. 7(b). The setup consists of transmitting and receiving LP standard-gain horn antennas with two lenses in between. The fabricated sample sits one focal length away from each lens such that the phase front of the wave impinging on the sample mimics that of a plane wave. On the other hand, the output of each horn antenna is modeled as a Gaussian beam and the optimal distance between the horn antennas is calculated to be 400 mm [42]. Before the measurement, the system is calibrated by the standard two-port through-reflect-line calibration, where a metal plate is used as the reflection standard at the location of the sample, while the reference

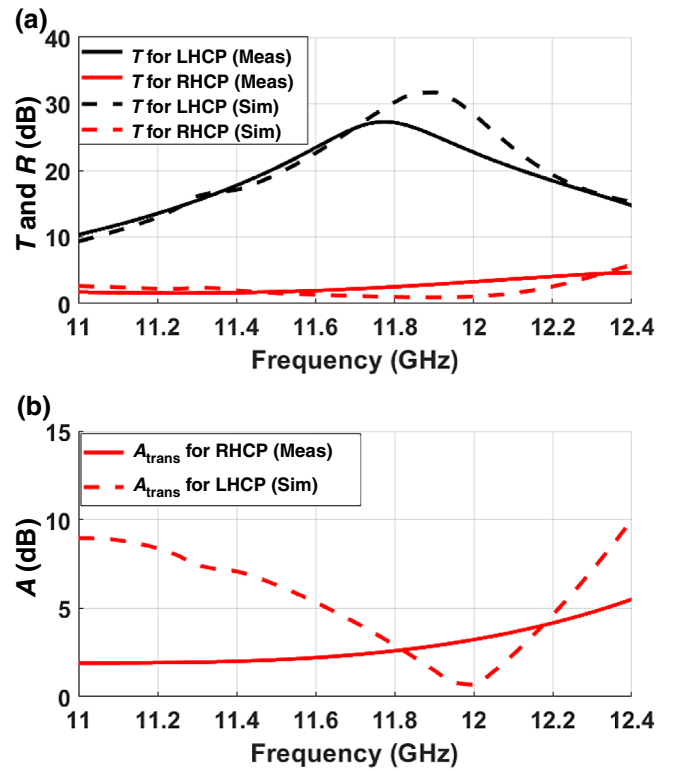


FIG. 8. The experimental results. (a) Comparison between the measured T (solid curves) and simulated T (dotted curves) for the transmitted RHCP and LHCP fields. (b) The measured (solid curve) and simulated (dotted curve) axial ratios of the transmitted RHCP field.

plane of the sample is defined as “through.” To properly define a quarter-wavelength line, we place the antennas, lenses, and the sample on a micrometer translation stage. Once the system has been calibrated, we perform three separate measurements to measure the copolarized and cross-polarized transmission coefficients (i.e., S_{21}^{xx} , S_{21}^{yx} , and S_{21}^{yy}) by aligning the transmitting and receiving antennas, and rotating one of them by 90° with respect to the other. This allows us to completely characterize the transmission properties of the fabricated sample in terms of LP waves. In each measurement, we apply time gating for all of the measured scattering parameters to filter out the unwanted reflections from the lenses and horn antennas. The measured transmission coefficients are then converted to a CP basis by use of Eq. (16), and the corresponding T , R , and A are computed and are compared with the simulated values in Fig. 8. As seen, the measured T for a RHCP field closely matches the simulated values, where the measured T is 1.76 dB at 11.5 GHz. The shift in the operating frequency may be attributed to fabrication imperfections. Additionally, the measured T for a LHCP field also closely matches the simulated values, where the measured value is 20.34 dB at 11.5 GHz. As expected, there is a large difference in the transmission of the two orthogonal CP fields,

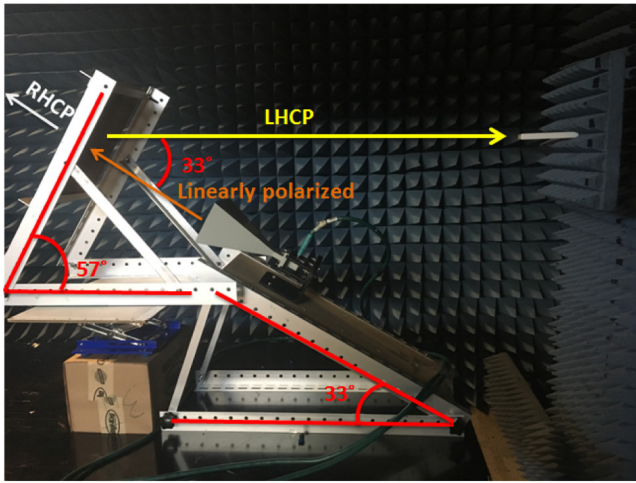


FIG. 9. The near-field measurement setup.

which also agrees with the full-wave-simulation results shown in Figs. 6(a) and 6(b). On the other hand, the A of the transmitted RHCP field does not perfectly align with the simulated values. This may be attributed to any phase errors that occur when we are positioning the metal plate for defining the reflection standard since any slight deviation translates to large artificial reflection and transmission phases. Nevertheless, the measured A is still below 3 dB at 11.5 GHz (2.08 dB).

To measure the reflection properties of the fabricated sample, the quasioptical measurement setup is inappropriate because an incident LHCP field is expected to be reflected at 33° off broadside, while all of the apparatuses are mounted on a straight micrometer translation stage. As such, we use a near-field measurement system from NSI-MI Technologies to measure the reflected LHCP field as shown in Fig. 9. Here we slant the feed antenna at 33° , while the fabricated sample is tilted at 57° such that the feed will normally impinge the sample and the reflected LHCP field will align with the near-field probe. The feed is a LP standard-gain horn antenna; hence, a single measurement characterizes the reflection properties of the sample for a LHCP field and a RHCP field. Figure 10 shows a summary of the far-field amplitude distributions for the reflected LHCP and RHCP fields at 11.5 GHz. As shown in Fig. 10(a), near the center of the scan range, we see a distinct beam of LHCP field. In contrast, we do not observe a clear beam for a RHCP field, as shown in Fig. 10(b). In particular, Fig. 10(c) shows a cut along the elevation angle at an azimuth angle of 0° . Whereas a clear beam is observed for the reflected LHCP field, the amplitude of the RHCP field is well below -60 dB for all elevation angles. The difference between the amplitudes of the reflected LHCP and RHCP fields at the center of the scan range is 20 dB. As such, the fabricated sample indeed reflects an incident LHCP field at 33° off broadside while transmitting most

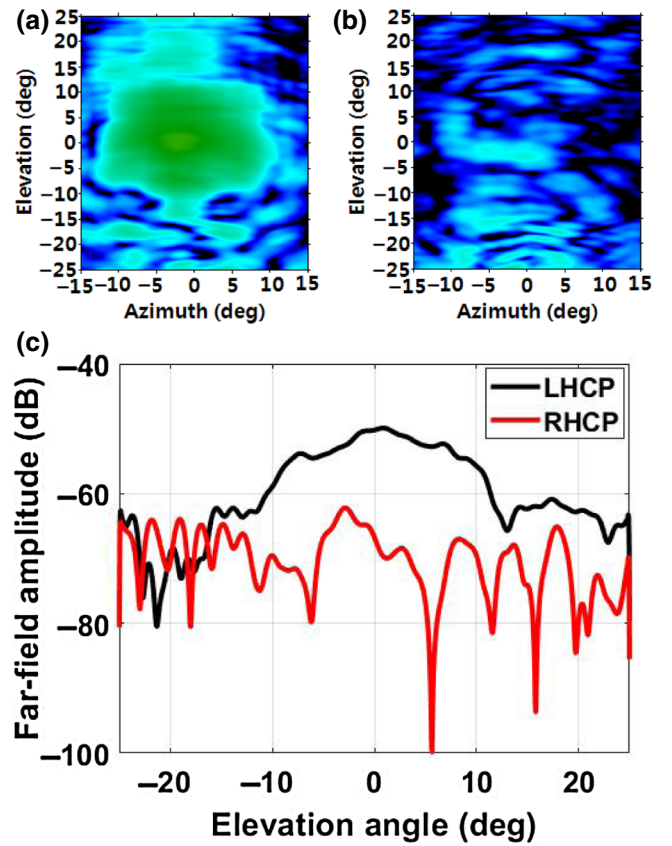


FIG. 10. The measured far-field amplitude distributions. The reflected (a) LHCP field and (b) RHCP field. (c) The far-field amplitude along a cut for an azimuth angle of 0° .

of an incident RHCP field, as verified by the quasioptical measurement.

IV. CONCLUSION

We propose and experimentally demonstrate an impedance-matched CPSS that also offers spin-selective phase modulation in the microwave regime. In particular, we cascade four tensor impedance layers to first realize an impedance-matched CPSS. These tensor impedance layers encode particular impedance values, which allow the impedance-matching condition to be satisfied for one handedness of a CP field, while maximizing the reflection for the opposite handedness. A numerical synthesis technique for obtaining the required impedance values is discussed in detail on the basis of the multiconductor-transmission-line system. Additionally, we propose crossed meander lines as our unit cell for implementation of the required impedance values at the operating frequency of 12 GHz. On the other hand, a spin-selective phase modulation is achieved by realization of a phase difference of 180° between the copolarized reflection coefficients of the devised CPSS, thereby leveraging the theory of Pancharatnam-Berry phase shift. We

experimentally demonstrate the proposed concept by using a free-space quasioptical setup and a near-field measurement system to confirm nearly reflectionless transmission of a RHCP field and anomalous reflection of a LHCP field, respectively, at 12 GHz.

ACKNOWLEDGMENTS

We thank Professor Sean V. Hum for allowing us to use the near-field measurement system and Dr. Elham Baladi for her guidance in accessing the system. We also thank Rogers Corporation for providing Rogers 5880 substrate samples.

APPENDIX: MUTUAL-COUPLING ANALYSIS

The proposed numerical synthesis method in Sec. II A assumes that a unit cell supports only two fundamental propagating Floquet modes such that there is no mutual coupling between the impedance layers. However, the proposed physical unit cell has finite periodicity ($T = \lambda/5.5$) and hence higher-order Floquet modes are inevitably present. Nevertheless, because of the subwavelength unit-cell periodicity, these higher-order modes are evanescent waves. As such, provided that the physically realized impedance layers are sufficiently far apart from each other, the proposed numerical synthesis method in Sec. II A is not affected by this mutual coupling. To determine the minimum separation distance that gives negligible mutual coupling, two cascaded unit cells are simulated for various separation lengths. Figure 11 shows the variations in the magnitudes of the net scattering parameters ($|S_{11}^{xx}|$, $|S_{11}^{yy}|$, $|S_{12}^{xx}|$, and $|S_{12}^{yy}|$) as a function of the separation length (the other scattering parameters are not shown to

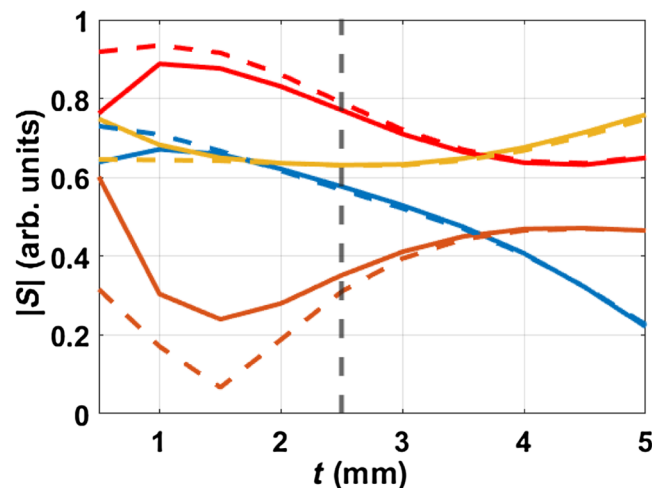


FIG. 11. Comparison between the simulated and analytical scattering parameters for two cascaded unit cells with variable separation length, t . The blue, orange, brown, and red curves correspond to the variations in $|S_{11}^{xx}|$, $|S_{11}^{yy}|$, $|S_{12}^{xx}|$, and $|S_{12}^{yy}|$, respectively.

avoid cluttering the figure). In Fig. 11, the dashed curves show the results from the analytical calculations [Eq. 12], which assume that there is no mutual coupling between the impedance layers. On the other hand, the solid curves show the full-wave-simulation results, which include the mutual coupling effect from higher-order Floquet modes. It is seen that for substrate thicknesses less than 2.5 mm, the analytical model and full-wave simulation do not perfectly match. This implies that substrates thinner than 2.5 mm do not sufficiently suppress higher-order Floquet modes and lead to mutual coupling. In contrast, for substrate thicknesses greater than 2.5 mm, the analytical model now accurately predicts the net scattering parameters of the cascaded system. In the proposed design, we set the separation distance to be 3.175 mm. Therefore, such a separation distance is sufficient for suppressing unwanted higher-order Floquet modes and the proposed theory is applicable to the physical design used in this work.

- [1] N. Yu, P. Genevet, M. A. Kats, F. Aieta, J. Tetienne, F. Capasso, and Z. Gaburro, Light propagation with phase discontinuities: Generalized laws of reflection and refraction, *Science* **334**, 333 (2011).
- [2] M. Selvanayagam and G. V. Eleftheriades, Discontinuous electromagnetic fields using orthogonal electric and magnetic currents for wavefront manipulation, *Opt. Express* **21**, 14409 (2013).
- [3] N. Yu, P. Genevet, F. Aieta, M. A. Kats, R. Blanchard, G. Aoust, J. Tetienne, Z. Gaburro, and F. Capasso, Flat optics: Controlling wavefronts with optical antenna metasurfaces, *IEEE J. Sel. Top. Quantum Electron.* **19**, 4700423 (2013).
- [4] F. Monticone, N. M. Estakhri, and A. Alù, Full Control of Nanoscale Optical Transmission with a Composite Metascreen, *Phys. Rev. Lett.* **110**, 203903 (2013).
- [5] Minseok Kim, Alex M. H. Wong, and George V. Eleftheriades, Optical Huygens' Metasurfaces with Independent Control of the Magnitude and Phase of the Local Reflection Coefficients, *Phys. Rev. X* **4**, 041042 (2014).
- [6] D. Lin, P. Fan, E. Hasman, and M. L. Brongersma, Dielectric gradient metasurface optical elements, *Science* **345**, 298 (2014).
- [7] I. V. Semchenko, S. A. Khakhomov, and A. L. Samofalov, Helices of optimal shape for nonreflecting covering, *Eur. Phys. J. Appl. Phys.* **49**, 33002 (2010).
- [8] J. P. S. Wong, A. Epstein, and G. V. Eleftheriades, Reflectionless wide-angle refracting metasurfaces, *IEEE Antennas Wirel. Propag. Lett.* **15**, 1293 (2016).
- [9] X. Ni, N. K. Emani, A. V. Kildishev, A. Boltasseva, and V. M. Shalaev, Broadband light bending with plasmonic nanoantennas, *Science* **335**, 427 (2012).
- [10] X. Ni, A. V. Kildishev, and V. M. Shalaev, Metasurface holograms for visible light, *Nat. Commun.* **4**, 2807 (2013).
- [11] L. Huang, X. Chen, H. Mühlenbernd, H. Zhang, S. Chen, B. Bai, Q. Tan, G. Jin, K. Cheah, C. Qiu, J. Li, T. Zentgraf, and S. Zhang, Three-dimensional optical holography using a plasmonic metasurface, *Nat. Commun.* **4**, 2808 (2013).

- [12] Minseok Kim, Junho Jeong, Joyce K. S. Poon, and George V. Eleftheriades, Vanadium-dioxide-assisted digital optical metasurfaces for dynamic wavefront engineering, *J. Opt. Soc. Am. B* **33**, 980 (2016).
- [13] Ching-Fu Chen, Chen-Ta Ku, Yi-Hsin Tai, Pei-Kuen Wei, Heh-Nan Lin, and Chen-Bin Huang, Creating optical near-field orbital angular momentum in a gold metasurface, *Nano Lett.* **15**, 2746 (2015).
- [14] Fan Bi, Zhongling Ba, and Xiong Wang, Metasurface-based broadband orbital angular momentum generator in millimeter wave region, *Opt. Express* **26**, 25693 (2018).
- [15] Haoran Ren, Gauthier Briere, Xinyuan Fang, Peinan Ni, Rajath Sawant, Sébastien Héron, Sébastien Chenot, Stéphane Vézian, Benjamin Damilano, Virginie Brändli, Stefan A. Maier, and Patrice Genevet, Metasurface orbital angular momentum holography, *Nat. Commun.* **10**, 2986 (2019).
- [16] Nanfang Yu, Francesco Aieta, Patrice Genevet, Mikhail A. Kats, Zeno Gaburro, and Federico Capasso, A broadband, background-free quarter-wave plate based on plasmonic metasurfaces, *Nano Lett.* **12**, 6328 (2012).
- [17] A. Pors and S. I. Bozhevolnyi, Efficient and broadband quarter-wave plates by gap-plasmon resonators, *Opt. Express* **21**, 2942 (2013).
- [18] Xiaoxiao Wu, Yan Meng, Li Wang, Jingxuan Tian, Shiwei Dai, and Weijia Wen, Anisotropic metasurface with near-unity circular polarization conversion, *Appl. Phys. Lett.* **108**, 183502 (2016).
- [19] J. Sanz-Fernández, E. Saenz, and P. de Maagt, A circular polarization selective surface for space applications, *IEEE Trans. Antennas Propag.* **63**, 2460 (2015).
- [20] Y. Zhao, M. A. Belkin, and A. Alù, Twisted optical metamaterials for planarized ultrathin broadband circular polarizers, *Nat. Commun.* **3**, 870 (2012).
- [21] Yang Zhao, Jinwei Shi, Liuyang Sun, Xiaoqin Li, and Andrea Alù, Alignment-free three-dimensional optical metamaterials, *Adv. Mater.* **26**, 1439 (2014).
- [22] Ying-Hua Wang, Jian Shao, Jie Li, Ming-Jie Zhu, Jiaqi Li, and Zheng-Gao Dong, Unidirectional cross polarization rotator with enhanced broadband transparency by cascading twisted nanobars, *J. Opt.* **18**, 055004 (2016).
- [23] M. Selvanayagam and G. V. Eleftheriades, Polarization control using tensor Huygens' surfaces, *IEEE Trans. Antennas Propag.* **62**, 6155 (2014).
- [24] M. Selvanayagam and G. V. Eleftheriades, Design and measurement of tensor impedance transmitarrays for chiral polarization control, *IEEE Trans. Microw. Theory Tech.* **64**, 414 (2016).
- [25] A. Ericsson and D. Sjöberg, Design and analysis of a multi-layer meander line circular polarization selective structure, *IEEE Trans. Antennas Propag.* **65**, 4089 (2017).
- [26] Amin Ranjbar and Anthony Grbic, Broadband, Multiband, and Multifunctional All-Dielectric Metasurfaces, *Phys. Rev. Appl.* **11**, 054066 (2019).
- [27] Minseok Kim and George V. Eleftheriades, Design and demonstration of impedance-matched dual-band chiral metasurfaces, *Sci. Rep.* **8**, 3449 (2018).
- [28] C. Cappellin, D. Sjöberg, A. Ericsson, P. Balling, G. Gerini, N. J. G. Fonseca, and P. De Maagt, in *2016 10th European Conference on Antennas and Propagation (EuCAP)* (IEEE, Davos, Switzerland, 2016), p. 1.
- [29] M. Zhou and S. B. Sørensen, in *2016 10th European Conference on Antennas and Propagation (EuCAP)* (IEEE, Davos, Switzerland, 2016), p. 1.
- [30] Liqiao Jing, Zuoqia Wang, Renuka Maturi, Bin Zheng, Huaping Wang, Yihao Yang, Lian Shen, Ran Hao, Wenyan Yin, Erping Li, and Hongsheng Chen, Gradient chiral metamirrors for spin-selective anomalous reflection, *Laser Photon. Rev.* **11**, 1700115 (2017).
- [31] Yang Chen, Xiaodong Yang, and Jie Gao, Spin-controlled wavefront shaping with plasmonic chiral geometric metasurfaces, *Light: Sci. Appl.* **7**, 84 (2018).
- [32] Zhijie Ma, Yi Li, Yang Li, Yandong Gong, Stefan A. Maier, and Minghui Hong, All-dielectric planar chiral metasurface with gradient geometric phase, *Opt. Express* **26**, 6067 (2018).
- [33] H. R. Phelan, Spiraphase – A new, low-cost, lightweight phased array, *Microw. J.* **19**, 41 (1976).
- [34] M. Kim and G. V. Eleftheriades, in *2019 IEEE International Symposium on Antennas and Propagation USNC/URSI National Radio Science Meeting* (IEEE, Atlanta, GA, USA, 2019).
- [35] Minseok Kim and George V. Eleftheriades, Highly efficient all-dielectric optical tensor impedance metasurfaces for chiral polarization control, *Opt. Lett.* **41**, 4831 (2016).
- [36] Arun K. Bhattacharyya, in *Phased Array Antennas* (John Wiley & Sons, Inc., Hoboken, NJ, 2006), p. 187.
- [37] Viktor Liljegren, Master's thesis, School Lund University (2013).
- [38] Johan Lundgren, Master's thesis, School Lund University (2016).
- [39] S. Pancharatnam, Generalized theory of interference, and its applications, *Proc. Indian Acad. Sci. Sect. A* **44**, 247 (1956).
- [40] M. V. Berry, Quantal phase factors accompanying adiabatic changes, *Proc. R. Soc. London A. Math. Phys. Sci.* **392**, 45 (1984).
- [41] J. Y. Lau and S. V. Hum, Reconfigurable transmitarray design approaches for beamforming applications, *IEEE Trans. Antennas Propag.* **60**, 5679 (2012).
- [42] Paul F. Goldsmith, in *Quasioptical Systems: Gaussian Beam Quasioptical Propagation and Applications* (Wiley-IEEE Press, Piscataway, NJ, 1998), p. 157.